AIAA JOURNAL
Vol. 33, No. 4, April 1995

Investigation of Supersonic Flow About Strut/Endwall Intersections in an Annular Duct

K. E. Williams*
University of Washington, Seattle, Washington 98195
G. J. Harloff†
Sverdrup Technology, Inc., Brook Park, Ohio 44142
and
F. B. Gessner‡
University of Washington, Seattle, Washington 98195

A combined experimental and numerical study was conducted to investigate the nature of supersonic turbulent flow past an array of four, circumferentially equidistant, diamond-shaped struts which spanned the width of an annular, constant area duct. The validity of the experimental and numerical techniques is demonstrated by comparing predicted and measured duct wall static pressure, pitot pressure, and limiting surface streamlines. The computations and experiments both indicate a complex shock structure which persists many chord lengths downstream of the strut. The computations and experiments also reveal the existence of horseshoe-type vortices which are generated at the leading and trailing edges of the struts. Corner vortices are generated at the intersections of both the compression and expansion faces of the struts with the duct walls.

Nomenclature

c = strut chord length
M = Mach number
P = static pressure
P_t = total pressure
P_{t2} = pitot pressure
P_o = reference upstream total pressure
r = radial coordinate measured from the duct centerline
u_τ = friction velocity, $(\tau_w/\rho_w)^{\frac{1}{2}}$
x = axial coordinate measured from the strut leading edge
y = coordinate normal to the endwall
y^+ = law-of-the-wall coordinate, (yu_τ/ν_w)
Δr = radial coordinate measured outward from the centerbody
θ = circumferential coordinate measured from the strut chordline
ν_w = kinematic viscosity at the wall
ρ_w = density at the wall
τ_w = shear stress at the wall

Introduction

THREE-DIMENSIONAL shock/boundary-layer interactions in supersonic flow caused by fin/endwall intersections have been studied extensively for several decades. McCabe[1] and Korkegi[2] used oil flow techniques and surface pressure measurements to develop a three-dimensional "separation" criterion for single-fin/flat-plate interactions. (The terminology "single-fin/flate-plate interaction" is intended to be a "label" for the flowfield about a single-fin/flate-plate intersection. Similar labeling of other interaction types occurs thoughout this paper.) Kubota and Stollery[3] proposed a flow model for this type of interaction on the basis of their surface pressure and smoke screen data. Settles and Lu,[4] Settles and Kimmel,[5] Settles and Dolling,[6] and Alvi and Settles[7] established a more complete flow model using various experimental techniques and pioneered the development of similarity and scaling laws, which Lu[8] has recently confirmed by means of endwall surface pressure measurements. Mee et al.[9] measured static pressures and used an oil flow technique to visualize limiting streamlines on the endwall to quantify multiple and single-fin/flat-plate interactions. In a more recent work, Koide and Stollery[10] employed schlieren and laser-light sheet flow visualization techniques to investigate the influence of strake and fillet modifications on the sharp-fin/flat-plate interaction. Shizawa et al.[11] have recently investigated the effect of bleed on reducing the size of the horseshoe vortex generated immediately upstream of the fin/plate intersection. Computational studies of the sharp-fin/flat-plate interaction have clarified the nature of the separation and attachment processes that occur on the plate surface, specifically with respect to horseshoe vortex formation and secondary separation beneath this vortex.[12–14] Recent predictions by Panaras[15] and Knight et al.[16] have confirmed the flow model for the interaction proposed by Alvi and Settles.[7]

In reference to blunt-fin/flat-plate interactions, computations performed by Hung and Buning[14] show that the resulting bow shock causes the boundary layer to separate well upstream of the fin, leading to bifurcation of the horseshoe vortex and formation of a lambda shock structure ahead of the fin. Subsequent computations by Lakshmanan and Tiwari[17] indicate that the magnitude of vorticity in the horseshoe vortex can be significantly reduced by proper filleting. In a recent series of papers, Brusniak and Dolling,[18] Erengil and Dolling,[19] and Kleifges and Dolling[20] have shown that the blunt-fin/flat-plate interaction is characterized by an unsteady separation shock pattern upstream of the blunt leading edge. Their results indicate that sweepback can have a beneficial effect by reducing the extent of the intermittently separated region ahead of the fin and the magnitude of rms pressure loading at the fin/plate intersection.[20]

Multiple-fin/endwall interactions, i.e., crossing-shock-wave/boundary-layer interactions, have been studied experimentally using surface pressure measurements and oil flow visualization by Bogdonoff and Stokes[21] and Williams and Hingst,[22] whereas Davis and Hingst[23] have made pitot pressure measurements in the crossing-shock flowfield. Garrison and Settles[24,25] have employed laser-sheet and surface flow techniques to visualize the shock patterns and flowfield of a multiple-fin/endwall interaction. Local skin-friction behavior in this type of interaction was examined by Garrison and Settles[26] in a subsequent study. Recently, Narayanswami et al.[27] and Reddy[28] have studied the crossing-shock problem numerically.

Presented as Paper 93-1925 at the AIAA/SAE/ASME/ASEE 29th Joint Propulsion Conference, Monterey, CA, June 28–30, 1993; received May 26, 1994; revision received Nov. 23, 1994; accepted for publication Dec. 6, 1994.

*Graduate Research Associate, Department of Mechanical Engineering. Student Member AIAA.

†Senior Staff Scientist; currently Staff Engineer, NYMA, Inc., Brook Park, OH 44142. Associate Fellow AIAA.

‡Professor, Department of Mechanical Engineering. Member AIAA.

On the basis of results generated in previous studies, fin/flat-plate interactions can be predicted with reasonable accuracy for semi-infinite compression fins. Some advanced supersonic propulsion concepts, however, require axially symmetric, annular inlets. In this case, curvature of the inlet walls may be an important factor. Furthermore, supersonic flow may exist over significant distances in these inlets, requiring the use of support struts within the supersonic flowfield (as opposed to traditional supersonic inlets, which typically have support structures located downstream of the normal shock). Understanding the impact of these finite-length support struts on the flowfield is important. The effects of endwall curvature and finite-length struts on the flowfield have not yet been considered in the available literature. The objective of the present study is to examine these effects to develop a more complete understanding of supersonic inlet aerodynamics. The emphasis is on the vortex structure and interactions generated by finite length fins (struts) placed 90 deg apart in an annular duct. In previous studies of supersonic flow along the intersection of a semi-infinite, sharp compression fin with a planar endwall, the presence of both a free-layer-type vortex and a corner vortex originating near the start of the intersection has been observed.[2–9,15,16] These vortices correspond, respectively, to the leading-edge horseshoe vortex and the compression face corner vortex upstream of the strut midchord. The present study will examine how these vortices behave and influence the flow and how additional vortices are formed as a result of the expansion process at the strut midchord and the recompression process at the trailing edge. These vortices are designated, respectively, as the expansion face corner vortex and the trailing-edge horseshoe vortex. The effect of strut thickness-to-chord ratio on the overall flowfield is investigated numerically in a companion paper by Harloff et al.[29]

Experimental Approach

The experimental measurements were made in the Department of Mechanical Engineering's supersonic annular flow facility at the University of Washington, which is discussed in more detail by Williams et al.[30] This facility operates continuously and consists of a plenum chamber, annular nozzle, and test section connected to a diffuser that exhausts into a large vacuum tank. Dry filtered air enters the plenum (stagnation) chamber where it passes through several flow conditioners. The annular convergent/divergent nozzle accelerates the flow to a nominal core flow Mach number of 3 at the nozzle exit. Boundary-layer trips were installed in the convergent section of the nozzle, as shown in Fig. 1, to promote turbulent boundary-layer development throughout the rest of the nozzle and test section. The test section of the facility starts at the nozzle exit and maintains a constant annular cross-sectional shape downstream. The outer wall diameter is 118.54 mm, whereas the inner wall diameter is 82.98 mm, creating a 0.7 inner-wall-to-outer-wall radius ratio. Four symmetric, unswept, diamond-shaped struts were positioned circumferentially equidistant in the test section at zero angle of attack, with their leading edges positioned 50.8 mm from the nozzle exit. The strut chord was 25.4 mm, yielding a strut height-to-chord ratio of 0.7; the maximum strut thickness was 0.125 chord lengths, corresponding to a 7.1 deg half-wedge angle. The Reynolds number, based on the strut chord, was 3×10^5. Pitot pressures were measured at axial positions of 0.5, 1.0, 2.0, 3.0, 4.0, and 6.0 chord lengths downstream from the leading edge of the strut.

Two pitot probes were used to make measurements near the inner and outer walls. Both probes had a round cross section at the tip with an outer diameter of 0.305 mm. Round tips were used instead of flattened tips (as are commonly used in two-dimensional boundary-layer surveys) because of the potential for significant pressure gradients in both perpendicular directions (r and θ) at the probe tip. The ratio of probe tip diameter to upstream boundary-layer thickness of the undisturbed flow was about 0.10 for both probes. Allen[31] has shown that a ratio of this magnitude results in no more than a 2% error in measured pitot pressure throughout the boundary layer. Measurements were made near the appropriate wall for the particular probe with some overlap in the core region to verify that the two probes were reading the same pressure. Both probes were aligned in the axial direction and no attempt was made to account for misalignment with the local flow direction. Strack[32] has shown that the pitot pressure sensed by a probe in a supersonic flow is relatively unaffected by flow angle; that is, an error of no more than 2% exists for flow angles up to 10 deg. This finding was confirmed for the probes used in the present study. Inasmuch as most flow angles at locations where pitot pressure data were taken are less than 10 deg, the maximum estimated error is on the order of 2%.

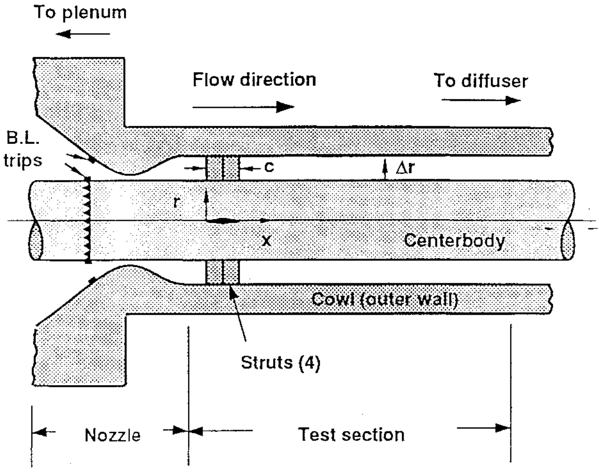

Fig. 1 Tunnel schematic.

Wall static pressures were measured at 0.0, 1.0, 2.0, 3.0, 4.0, 5.0, 6.0, 7.0, and 8.0 chord lengths behind the leading edge in 15-deg increments circumferentially on the inner wall and in 5-deg increments circumferentially on the outer wall. The wall pressure taps had an orifice diameter of 0.343 mm and were oriented normal to the wall. Williams et al.[30] discuss the pressure measurement techniques in more detail.

Limiting streamlines on the centerbody and the strut were experimentally determined using the fluorescent oil technique discussed by Chan.[33] Fluorescent dye, No. 50 yellow, mixed with silicon oil, was painted on the centerbody and strut in a thin film with a camel's hair brush. The facility was run for 60 s and then stopped suddenly to minimize the distortion of the oil pattern on the surfaces as the flow velocity decreased to zero in the test section.

Numerical Approach

The computations were performed for the geometry and flow conditions just described. The calculations were started 0.5 strut chord lengths ahead of the strut leading edge to account for the upstream influence of the strut in the subsonic part of the duct-wall boundary layers. The inflow boundary condition was prescribed from an axisymmetric calculation of the flow through the plenum, nozzle, and test section with no struts, as performed previously by the second author. Because the axisymmetric calculation was initiated upstream of the convergent/divergent nozzle, the initial conditions are based on a flow history similar to that of the experiment. The axisymmetric calculation agrees very well with preliminary results obtained from the experimental facility when no struts were installed (see Williams et al.[30]). The computed profiles were chosen as the inflow condition because mass and momentum could be conserved more accurately than by matching with experimental profiles upstream of the strut. Planes of symmetry at the strut centerplane and between struts were used to limit the computational domain, circumferentially, to one-eighth of the annular duct cross section. Figure 2 shows one of the computational grids investigated in this study, at every other grid point, as it appears on the bounding surfaces of the domain. The centerbody, cowl, and strut were treated as no-slip adiabatic surfaces. The boundary defined by the plane of symmetry of the strut, both ahead of the strut and behind, as well as the plane of symmetry between struts, were taken into account by extrapolating from the first grid plane inside of the boundary. The outflow boundary conditions at the exit plane were obtained by extrapolation from the adjacent interior grid plane.

PARC-3D,[34] a three-dimensional, Reynolds-averaged, Navier–Stokes flow solver, was used for the computations. In general, closure was obtained with the Baldwin–Lomax turbulence model[35]

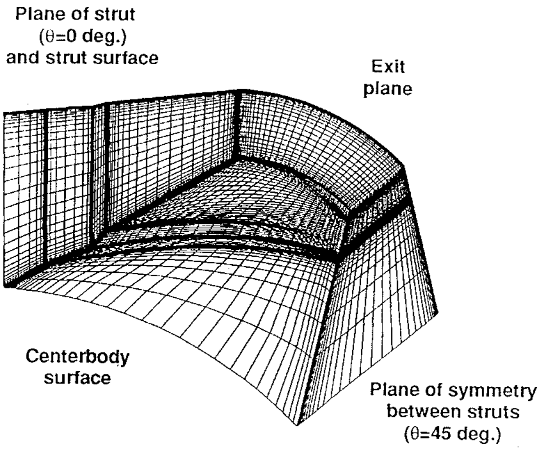

Fig. 2 Computational grid (147 × 51 × 51).

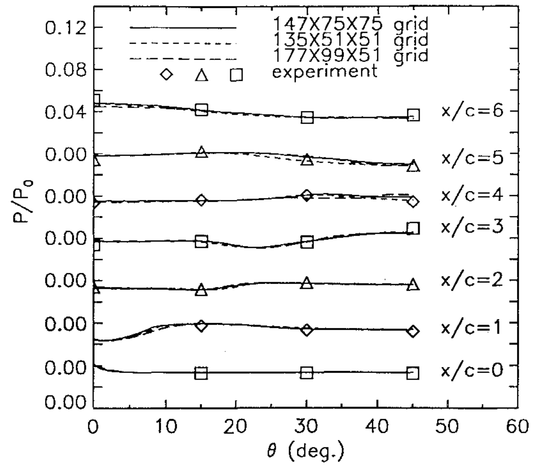

a) Static pressures on the centerbody

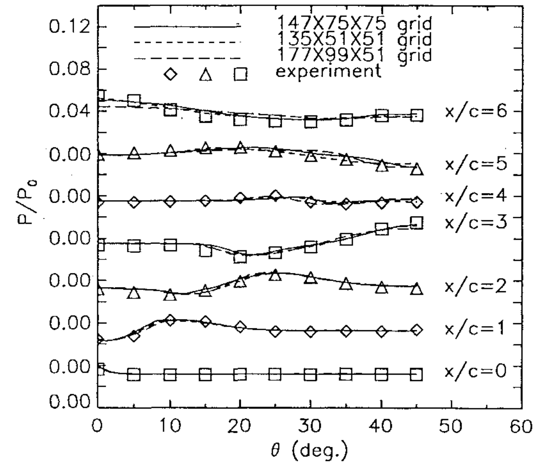

b) Static pressures on the cowl

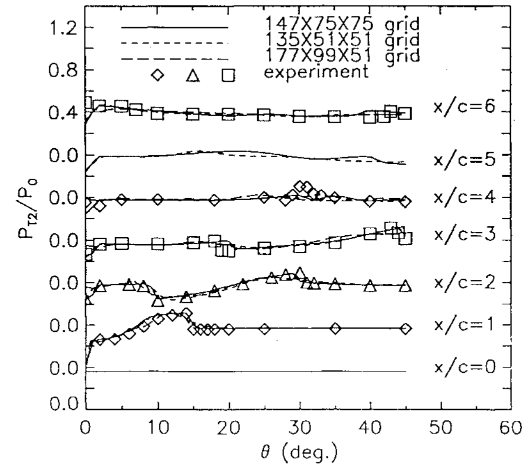

c) Pitot pressures at the gap midheight ($\Delta r/c$ = 0.35)

Fig. 3 Comparison of measured and computed pressures.

specified in regions of wall-bounded shear flow (the boundary layers), and with the Thomas turbulence model[36] in regions of free shear flow (the wake of the strut). The exception is the solution run on the first grid discussed later, for which the Baldwin–Lomax model was implemented throughout the entire flowfield.

Several grids were examined in this study. The first was created algebraically with hyperbolic clustering near the centerbody, cowl, and plane of symmetry of the strut. The dimensions of this grid were 177 × 99 × 51 nodes in the x, r, and θ directions, respectively. The first grid point away from the endwalls (centerbody and cowl) was at a $y^+ = 0.1$ based on the boundary-layer profile at the inlet to the computational domain. The first grid point away from the strut was at a distance that corresponded to a $y^+ = 1.0$ based on the endwall boundary-layer profiles in the axial direction and a $y^+ = 0.1$ in the circumferential direction. The other grids were created using GRIDGEN[37] with the first grid point away from the inner and outer walls at a $y^+ = 1.0$ based on the inlet boundary-layer profiles. The spacing of the first grid point on the strut was taken to be the same physical dimension as that used for the annular walls. To resolve the shock structure better, the grids were optimized by clustering along anticipated shock positions. Slight grid clustering near the plane of symmetry between struts was also incorporated to improve the accuracy of the symmetry boundary condition and the resolution of the crossing shocks in this plane. The first grid of this type had 135 × 51 × 51 nodes in the x, r, and θ directions, respectively. The last grid considered, as shown in Fig. 2, had 147 × 75 × 75 nodes. This grid was further adapted using MAG3D.[38] MAG3D attempted to adapt the grid by clustering around pressure gradients present in the flow solution; however, its application had little effect on the overall grid structure or subsequent solutions.

Results and Discussion

Comparison of Pressures

The experimentally measured and computed circumferential wall static pressure distributions on the centerbody, normalized by the upstream total pressure, are shown in Fig. 3a at axial locations corresponding to $x/c = 0$ (the strut leading edge), $x/c = 1$ (the strut trailing edge), and at $x/c = 2, 3, 4, 5$, and 6. Three calculations are shown; each used the same flow solver on the different grids. The computed distributions compare well with the experimental distributions, with the 135 × 51 × 51 grid solution giving slightly better overall agreement at the various axial locations. Figure 3b shows circumferential static pressure distributions on the cowl at the same axial locations as those shown in Fig. 3a. Again, the overall agreement is good, with the 135 × 51 × 51 grid performing slightly better than the other two grids. It should be noted that the most striking difference between Figs. 3a and 3b is that the pressure variation is more severe on the cowl than on the centerbody. At $x/c = 3$, for example, the pressure on the centerbody is a minimum of 0.031 times the reference total pressure at a circumferential position of $\theta \simeq 22$ deg and a maximum of 0.048 at 45 deg. At $x/c = 3$ on the cowl, the circumferential positions of the minimum and maximum are about the same; however, the minimum is now 0.022 and the maximum is 0.055. This increase in maximum pressure may be explained by the following argument: As a shock wave propagates circumferentially away from the strut, the cowl is curving into the shock wave, compressing it. The centerbody, on the other hand, is curving away from the shock, forcing the flow to expand to remain in contact with the retreating wall. This explanation does not, however, account for the lower minimum pressure observed on the cowl in comparison to that observed on the centerbody.

The circumferential variation of pitot pressure along the annular gap midheight is shown in Fig. 3c at the various x/c locations. This region is in the core flow where viscous effects are minimal (except in the vicinity of the strut wake centered about $\theta = 0$ deg).

Figure 3c shows that the shock wave generated at the leading edge of the strut has propagated to $\theta \simeq 14, 29$, and 44 deg at $x/c = 1, 2$, and 3, respectively, where it then travels out of the plot domain at $\theta = 45$ deg. Here, a shock wave generated from the neighboring strut at $\theta = 90$ deg crosses the shock wave mentioned earlier and moves into the domain. At $x/c = 4$ the leading-edge shock wave from the neighboring strut is at $\theta = 30$ deg where it crosses the shock wave generated at the trailing edge of the original strut. At this point, the experimentally measured pitot pressure "spikes" to a maximum of 0.5 times the reference total pressure, which is much higher than the computed pressure of about 0.38–0.41, depending on the grid. The trailing-edge shock is seen to have propagated to $\theta \simeq 9, 19$, and 30 deg at $x/c = 2, 3$, and 4, respectively. It then moves out of the domain between $x/c = 5$ and 6, where the trailing-edge shock from the neighboring strut moves into the domain. At $x/c = 6$, the trailing-edge shock from the neighboring strut is at $\theta \simeq 42$ deg and the leading-edge shock has moved to $\theta \simeq 0$ deg, thus completing one "shock diamond" in the domain plotted. Both solutions for the $135 \times 51 \times 51$ and the $147 \times 75 \times 75$ grids compare well with the experimental results between $x/c = 1$ and 3. Downstream of $x/c = 3$, the agreement is not as good, with the $147 \times 75 \times 75$ grid solution comparing best with experiment. With few exceptions, the maximum deviation between any particular solution and the experiment is no more than 5%.

Pitot pressure profiles at $x/c = 0.5$ (the strut midchord location) along radial traverses at $\theta = 3, 5, 8, 30$, and 45 deg are shown in Fig. 4a. The experimental results are shown as different symbols for each of the two probes used and include measurements made at symmetric ($\pm\theta$) positions on both sides of the strut. Along each traverse, there are two sets of symbols that represent measurements made near the cowl and two sets of symbols that represent measurements made near the centerbody. The measurements made by both probes are nearly coincident in the overlap region. Similarly, measurements made on both sides of the strut at symmetric positions are in excellent agreement. The agreement between measurements and the computed profiles is extremely good, except near the shock wave, which is seen to exist at $\theta = 8$ deg. This shock appears as a discontinuity in the measured pressures near $\Delta r/c = 0.22$. The $147 \times 75 \times 75$ grid solution matches the shock jump and position, whereas the other two solutions show a much more gradual pressure rise. The $135 \times 51 \times 51$ grid solution, although "smearing" the shock, does predict the full pressure rise, whereas the $177 \times 99 \times 51$ grid solution is so smeared that the calculated pitot pressure never reaches the experimentally measured peak pressure. The smearing of the shock is a result of insufficient grid resolution near the shock position. The boundary layers on the centerbody (at $\Delta r/c = 0$) and the cowl (at $\Delta r/c = 0.7$) are clearly evident and are of nominally equal thickness. The profiles at $\theta = 30$ and 45 deg are similar to each other and represent the undisturbed boundary layers at this axial location, inasmuch as the presence of the strut has not yet been felt at these circumferential positions. Finally, it should be pointed out that there is a small bulge at the edge of the cowl boundary layer at $\theta = 8$ deg near $\Delta r/c = 0.6$. This is a result of a lambda shock structure and is generally present at the edges of both boundary layers just upstream of the leading-edge shock wave. The lambda shock structure is discussed in more detail later.

Similar pitot pressure profiles downstream of the strut trailing edge at $x/c = 2.0$ are shown in Fig. 4b for $\theta = 0, 6, 18, 30$, and 45 deg. In this figure, the leading-edge shock wave discussed earlier in Fig. 4a has propagated outward to $\theta = 30$ deg. At this location, both the $147 \times 75 \times 75$ and $135 \times 51 \times 51$ grid solutions compare extremely well with the experimentally observed pitot pressure distribution. The $177 \times 99 \times 51$ grid solution has almost completely smeared out the shock due to insufficient grid resolution at this location resulting from the orthogonal nature of this particular grid. The profile at $\theta = 18$ deg is representative of profiles through the expansion fan generated at the midchord of the strut. The characteristic of these profiles is the "dishlike" behavior observed in the central region of the duct. The profiles at $\theta = 45$ deg are essentially undisturbed. The profile at $\theta = 0$ deg is in the wake of the strut, one chord length downstream of the trailing edge. At this circumferential position, there are substantial differences between the computed and measured profiles and also between different computed profiles. As mentioned earlier, the $177 \times 99 \times 51$ grid solution uses the Baldwin–Lomax turbulence model[35] throughout the flow. The other solutions, which employed the Thomas turbulence model[36] in regions of free shear, should model the wake more realistically. There are, however, even differences between the two solutions that utilize this model. More specifically, neither of these two solutions compares well with the experimental profile at $\theta = 0$ deg. The reasons for the differences between the predicted and experimentally measured wake profiles are discussed in more detail later.

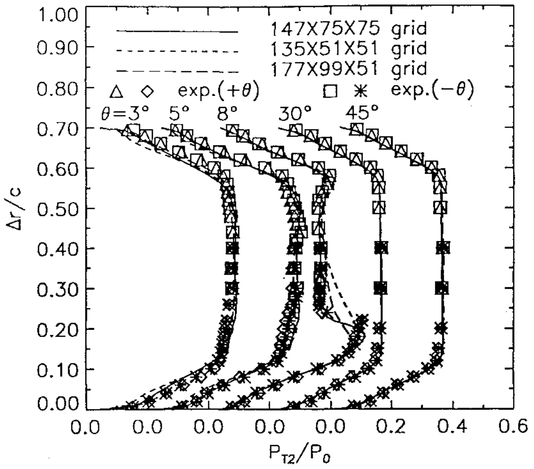

a) $x/c = 0.5$

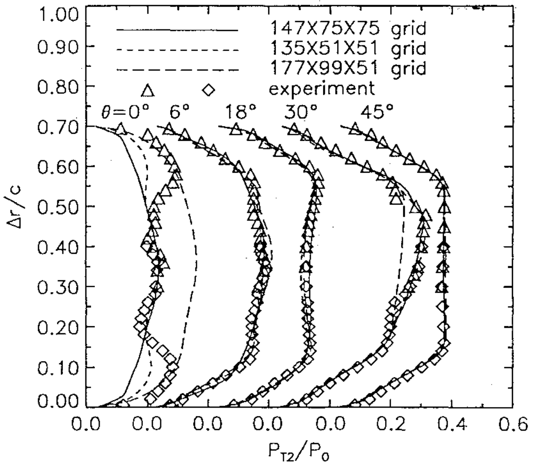

b) $x/c = 2.0$

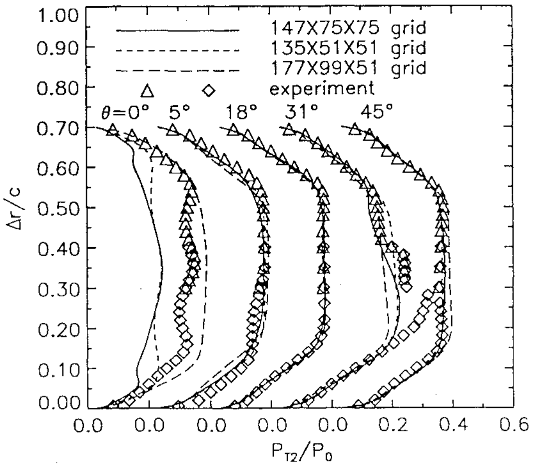

c) $x/c = 4.0$

Fig. 4 Comparison of measured and computed pitot pressures.

Pitot pressure profiles along radial traverses at $x/c = 4.0$ for $\theta = 0, 5, 18, 31$, and 45 deg are shown in Fig. 4c. This is the

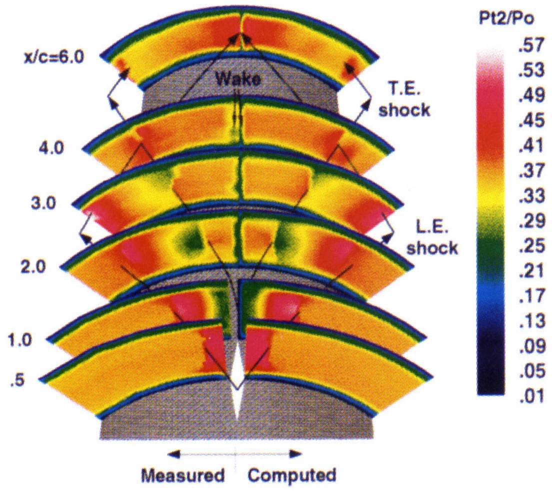

Fig. 5 Perspective view of measured and computed pitot pressures.

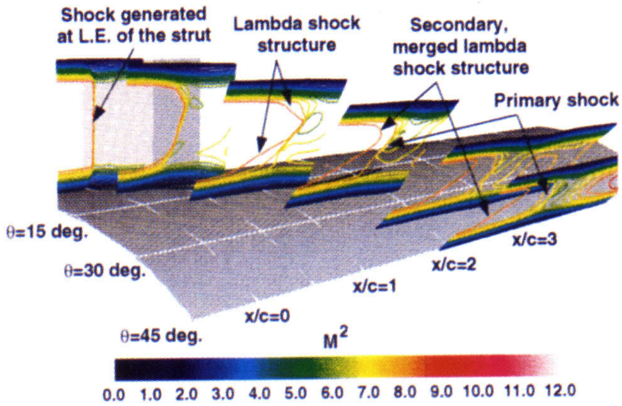

Fig. 6 Leading-edge shock propagation.

axial position where the leading-edge shock from the neighboring strut (positioned at $\theta = 90$ deg) crosses the shock generated at the trailing edge of the original strut (at $\theta = 0$ deg). This phenomenon is seen in the experimentally measured profile at $\theta = 31$ deg as two abrupt changes near $\Delta r/c = 0.30$ and 0.40. The computed profiles compare well with experiment except at this crossing position and in the wake.

Figure 5 shows a compilation of all of the measured pitot pressures in color bar form (plotted on the left) vs calculated pitot pressures from the 147 × 75 × 75 grid solution (plotted on the right). Subsequent figures include results that are based on this particular solution. In reference to Fig. 5, the propagation of the leading- and trailing-edge shock waves is clearly evident, as are the boundary layers on the cowl and centerbody surfaces. The differences between experimental and numerical results in the wake are evident in this figure. The experimentally observed wake includes two discreet "divots" in the pitot pressure behind the strut. It will be shown shortly that these divots are caused by two counter-rotating vortices formed in the corner of each strut compression face/endwall intersection (cowl and centerbody) that migrate away from each intersection before entering the wake. The numerical predictions severely underpredict the influence of these vortices on the downstream wake. The spreading angle of the measured wake is roughly 4 deg, which is much greater than that of the computed wake (approximately 1 deg).

Shock Structure

The computed development of the shock wave generated at the leading edge of the strut as it propagates toward the plane of symmetry between struts (at $\theta = 45$ deg) is shown in Fig. 6. The contour levels in this figure represent the square of the Mach number. Since the Mach number change across a shock wave is relatively small compared with the change across the boundary layer for this interaction, different contour levels of Mach number are concentrated primarily in the boundary layer. Squaring the Mach number exaggerates the differences across the shock waves while diminishing the changes in the boundary layer. The net effect is to displace contour lines away from the boundary layer, thus illustrating the shock structure more clearly. At the first circumferential position away from the strut, $\theta = 4$ deg, the shock wave extends linearly across the annular gap from cowl boundary layer to centerbody boundary layer. The shock wave can also be seen penetrating deep into both boundary layers. At the next position, $\theta = 8$ deg, the shock appears to bend forward just beyond both boundary layers but does not penetrate either boundary layer. This behavior is associated with early development of the lambda shock structure. By $\theta = 15$ deg, the shock wave clearly shows the characteristics of a lambda-type bifurcation just beyond the edge of each boundary layer. The triple point, or the point where the bifurcation occurs, for the centerbody lambda structure is slightly farther away from the centerbody boundary layer than the triple point for the cowl lambda structure. The lambda structures continue to grow as the shock moves circumferentially away from the strut, displacing the triple points farther into the core flow. By $\theta = 25$ deg, the two lambda structures have merged. As a result of this interaction, the presence of the strut is felt upstream of the propagating primary shock, even in the core flow where viscous effects are small. As this complicated shock structure continues to move away from the strut, the upstream extent of the secondary shock system formed by the merged lambdas moves farther upstream relative to the location of the propagating primary shock.

Comparison of Limiting Streamlines

Figure 7 shows experimentally measured and computed limiting streamlines on the centerbody as viewed from directly above a strut with the flow from left to right. The experimental limiting streamlines in Fig. 7a show good symmetry above and below the $\theta = 0$ deg line, which represents the plane of symmetry along the strut centerline. A line on a surface onto which adjacent limiting streamlines coalesce will be termed a "line of coalescence" and will be labeled C1, C2, etc. At a downstream location in the flow, coalescence of streamlines along this line may cease, but this line (now a limiting streamline itself) will retain its original label. In reference to the computed results in Fig. 7b, it can be seen that lines of coalescence emanate from the leading and trailing edges of the strut, C1 and C2, respectively. Beyond $x/c = 0.5$, coalescence of adjacent streamlines onto C1 is no longer observed. Similarly, beyond $x/c = 1.5$, adjacent streamlines no longer coalesce onto C2. The computed behavior of lines C1 and C2 in Fig. 7b agrees well with the surface oil flow pattern in Fig. 7a. The maximum circumferential penetration of computed line C1 is 20 deg at $x/c = 1.8$, which compares well with the oil flow results in Fig. 7a. The maximum penetration of computed line C2 is 12 deg at $x/c = 3.5$, which is somewhat less than that of its experimental counterpart. In reference to Fig. 7a, a third line of coalescence, C3, is observed experimentally that is not present in the computed results. This line originates at $x/c = 1.8$ and $\theta = 22$ deg, which is at a circumferential angle just greater than that of line C2 but less than the position of line C1. This third line of coalescence propagates outward until line C1 merges with it at $x/c = 2.8$ and $\theta = 16$ deg. The maximum circumferential propagation of this merged line is $\theta = 24$ deg at $x/c = 3.5$. The oil flow behind the lines of coalescence in Fig. 7a is observed to luminesce much less than that of the oil flows ahead of, and circumferentially beyond, the lines of coalescence when illuminated by ultraviolet light. This indicates that there is locally increased skin friction behind the lines of coalescence, inasmuch as the thickness of the oil film behind the lines of coalescence is thinner than elsewhere.

The static pressure distribution on the centerbody is also shown in Fig. 7b. The variations in static pressure may give some insight as to why the third line of coalescence would exist, inasmuch as there is a pressure rise present in Fig. 7b along the position of line C3 seen in Fig. 7a. This rise is similar to the pressure rise that occurs where C1 and C2 originate. Near the leading and trailing edges of the strut, there is a relatively rapid pressure rise associated with, and positioned nominally below, the shock waves generated there. Both lines of coalescence that emanate from the strut initially "ride" the pressure rise away from the strut. If the pressure rise at

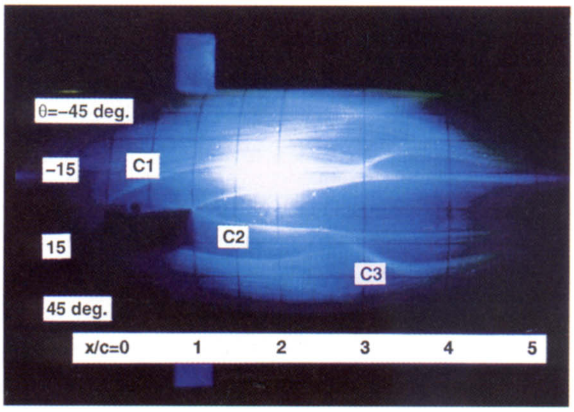

a) Experimentally observed limiting streamlines

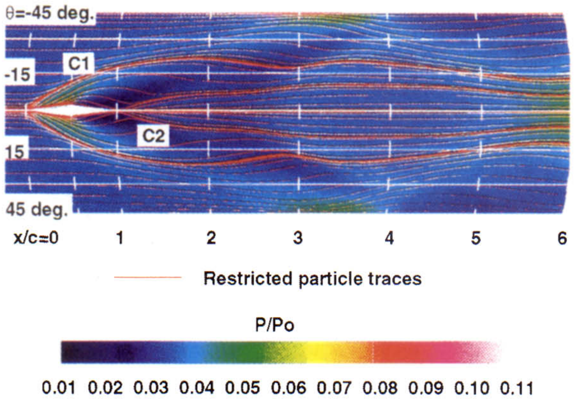

b) Computed limiting streamlines and static pressure

Fig. 7 Flow features on the centerbody.

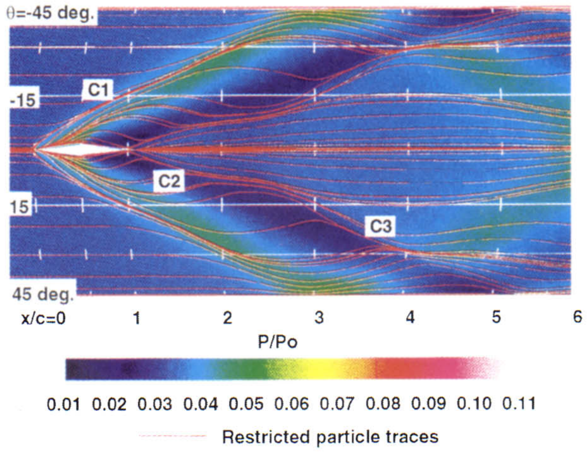

Fig. 8 Computed limiting streamlines and static pressure on the cowl.

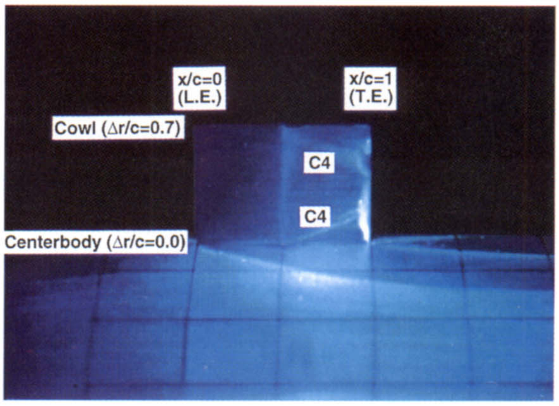

a) Experimentally observed limiting streamlines

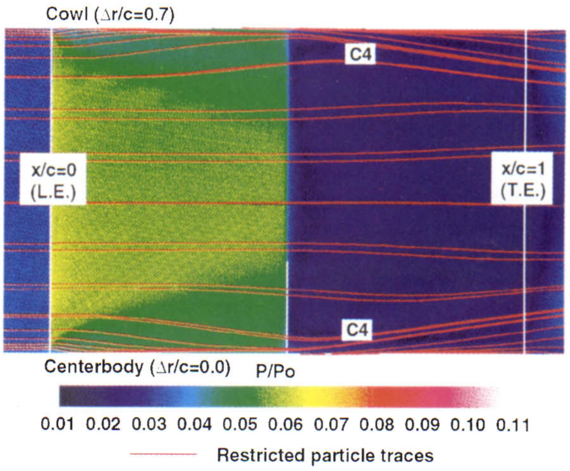

b) Computed limiting streamlines and static pressure

Fig. 9 Flow features on the strut.

the location of the third line of coalescence is sufficiently large, then this effect should generate another line of coalescence. The computations do not predict a third line of coalescence, however, which is possibly due to insufficient grid resolution. Aside from this behavior, the computed limiting streamlines generally agree well with the experimental results.

The computed limiting streamlines and static pressure distribution on the cowl are shown in Fig. 8. As with the centerbody, lines of coalescence are observed emanating from the leading and trailing edges of the strut. As mentioned earlier, static pressure variations on the cowl are clearly more severe than on the centerbody (compare with Fig. 7b). Similarly, the extent of the circumferential propagation of lines C1 and C2 is greater on the cowl than on the centerbody. More specifically, C1 reaches a maximum circumferential displacements of 33 deg at $x/c = 2.8$ on the cowl compared with 20 deg at $x/c = 1.8$ on the centerbody. Line C2 reaches 15 deg at $x/c = 4$ compared with 12 deg at $x/c = 3.5$. A third line of coalescence, C3, is observed to form at roughly $x/c = 3$ and $\theta = 18$ deg. This line, C3, is analogous to the experimentally observed third line of coalescence on the centerbody (refer to Fig. 7a). Because of difficulties in observation, no experimental results are available to compare with the computed limiting streamlines on the cowl.

The experimentally observed limiting streamlines on the strut are shown in Fig. 9a. A line of coalescence emanating from near the leading edge is inclined at a very shallow angle ($\simeq 2$ deg) relative to the centerbody along the compression face of the strut. When this line, C4, passes the strut midchord, the angle relative to the centerbody changes dramatically to roughly 18 deg. The computed limiting streamlines and static pressure distribution on the strut are shown in Fig. 9b. A line of coalescence, C4, is observed near the strut/centerbody intersection on the compression face of the strut, similar to that observed experimentally; however, when the computed line C4 passes the midchord, the angle of this line relative to the centerbody increases to only 6.5 deg, which is significantly less than that observed experimentally. Similar behavior is observed along the strut/cowl intersection. As will be discussed shortly, the lines of coalescence observed on the strut in Figs. 9a and 9b are related to the existence of compression face corner vortices.

Vortical Flow Structure

Computed particle traces (pathlines) near the centerbody and strut are shown in Fig. 10a. In this figure, black lines represent particle traces that have been restricted to the first computational plane away from the centerbody or the strut ($y^+ \simeq 1$). These traces represent limiting streamlines similar to those shown in Figs. 7b and 9b. Lines shown in red, yellow, or blue represent particle traces that are seeded

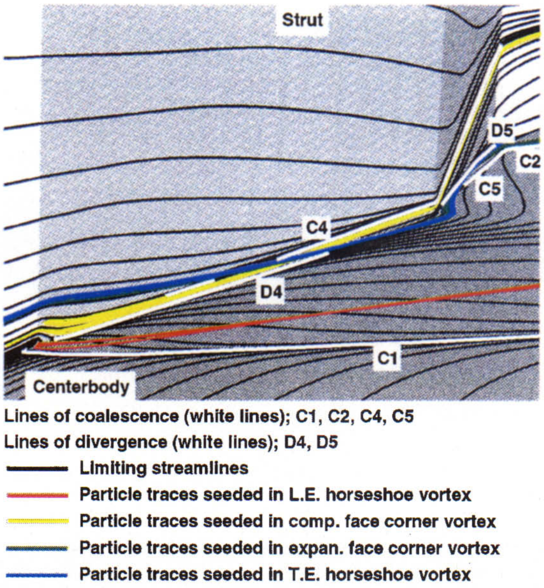

a) Along the intersection

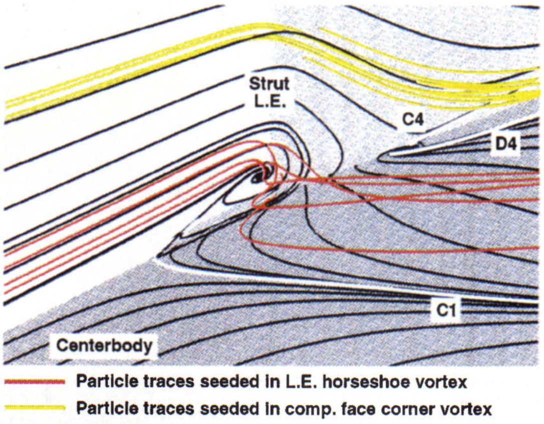

b) At the leading edge

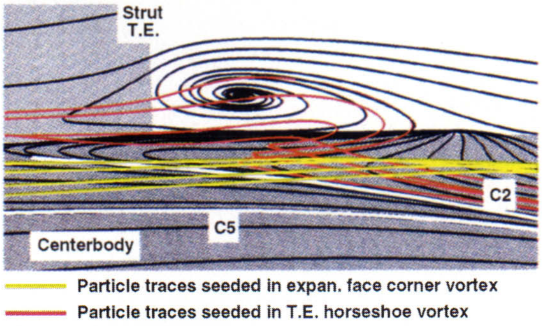

c) Near the trailing edge

Fig. 10 Computed pathlines at the strut/centerbody intersection.

with no restrictions on their motion, thus representing pathlines in the flow. Lines of coalescence (C) and divergence (D) are white lines to aid in visualization.

The compression face corner vortex is characterized by the line of coalescence, C4, on the strut and a line of divergence, D4, on the centerbody, whereas the expansion face corner vortex is characterized by a line of coalescence, C5, on the centerbody and a line of divergence, D5, on the strut. This indicates that there are two distinct vortices in the corner of the strut–endwall intersection that rotate in an opposite sense. These corner vortices are formed by transverse pressure gradients acting in the corner region, which cause the flow to migrate from the strut to the centerbody along the compression face and from the centerbody to the strut along the expansion face. The migrating flow near these surfaces cannot support the large changes in velocity associated with approaching a corner having infinitesimal curvature, and the flow separates from the surface just upstream of the corner, reattaching to the surface just downstream of the corner. The fluid in the corner under the migrating flow forms a corner vortex that is driven by the migrating fluid passing over it.

Figure 10b is an enlargement of the region near the leading edge of the strut, as shown in Fig. 10a. In this figure, particles seeded in the core of the leading-edge horseshoe vortex near the strut are traced in red. These traces are seen to travel away from the strut leading edge, traveling behind the line of coalescence, C1. Clearly, this line of coalescence represents a line of separation at the front of the leading-edge horseshoe vortex. The horseshoe vortex in subsonic strut–endwall flows wraps around the strut, but in a supersonic interaction, it "rides" away from the strut on the pressure rise caused by the shock wave. The vortex, as viewed on the centerplane of the strut immediately upstream of the strut/centerbody intersection in Fig. 10b, has a nominal diameter of $y^+ \simeq 9$ based on the inlet boundary-layer profile. This indicates that the vortex exists primarily within the viscous sublayer of the boundary layer where the flow is subsonic. This vortex is formed as vorticity in the incoming boundary layer is stretched by the divergence of the velocity field as the flow turns around the strut.

At the trailing edge, vorticity in the boundary layer will be stretched by the divergence of the velocity field as the flow responds to the recompression shock. In other words, the severe adverse pressure gradient induced by the recompression shock causes the flow to separate and vortex roll-up to occur in the subsonic portion of the boundary layer. This process creates a "horseshoe" vortex in a manner similar to that observed at the leading edge. In fact, a recirculation pattern is observed just behind the strut, as shown in Fig. 10c, which is an enlargement of the region near the trailing edge in Fig. 10a. Vortex roll-up and the outward spiraling limiting streamlines on the strut plane of symmetry in Fig. 10c are in the clockwise direction. Particles seeded in the trailing-edge horseshoe vortex near the trailing edge are traced in red in Fig. 10c. These traces are seen traveling just behind the line of coalescence, C2. This line of coalescence is, therefore, a line of separation associated with the trailing edge horseshoe vortex. The red particle traces in this figure were integrated forward and backward in time so that the pathlines could be determined upstream, as well as downstream, of the seeding point. The traces seeded in the trailing-edge horseshoe vortex are observed to arrive at the vortex via the expansion face corner vortex. Particles seeded near the core of the expansion face corner vortex, slightly upstream of the trailing edge, are traced in yellow in Fig. 10c. These traces show that the expansion face corner vortex remains bounded by the line of coalescence C5, which merges with C2 just downstream of the view shown by Fig. 10c. Furthermore, the yellow traces are turned circumferentially outward just downstream of the view in Fig. 10c joining up with the red traces. This behavior indicates that the trailing-edge horeshoe vortex is a separate vortex from the expansion face corner vortex, but the two vortices rapidly merge. The trailing-edge vortex has a nominal diameter of $y^+ \simeq 18$ on the center plane, which indicates that it is larger in size than the leading-edge horseshoe vortex. Behavior similar to that shown in Fig. 10 was observed for the leading- and trailing-edge vortices generated at the strut/cowl (outer duct wall) intersection.

Particles seeded in the compression face/centerbody corner vortex in Figs. 10a and 10b are traced in yellow. All particles seeded in the compression face/centerbody corner vortex are observed to be swept up the strut on the expansion face and deposited in the wake of the strut away from the centerbody (see Fig. 10a). Similar features were also observed at the strut/cowl intersection. As mentioned earlier, there are two distinct pitot pressure deficits in the experimentally observed wake, as illustrated by the results shown in Figs. 4b and 4c. These pressure deficits have radial positions, similar to those of the yellow traces in Fig. 10a, and particle traces seeded in the compression face/cowl corner vortex (not shown), downstream of the strut. It is speculated that the observed pitot pressure deficits

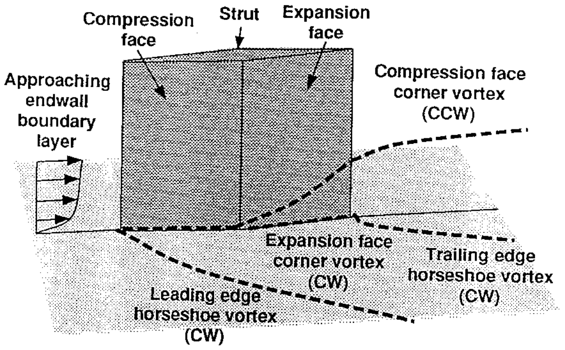

Fig. 11 Observed vortical flow pattern at a strut/endwall intersection in supersonic flow: CW, clockwise rotation as viewed from downstream; CCW, counter clockwise rotation as viewed from downstream.

are caused by the corner vortices, which propagate downstream of the strut trailing edge and distort the wake. Even though the particle traces are swept up the strut and occupy similar positions in the computations, the computed corner vortex dissipates shortly after it leaves the corner on the expansion face of the strut, which explains why the computed pitot pressure deficit in the wake, away from the endwall boundary layers, is not as distorted as that observed experimentally (refer to Fig. 5).

On the basis of the aforementioned results, it can be concluded that a multivortex flow pattern is generated at each strut/endwall intersection. This generalized vortex pattern is shown, with rotational directions, in Fig. 11. The overall pattern includes horseshoe vortices emanating from the leading and trailing edge of the strut/endwall intersection, as well as corner induced vortices at the compression face/endwall and the expansion face/endwall intersections. The compression face corner induced vortex is convected away from the corner on the expansion face of the strut by the crossflow in the corner region boundary layer, which has reversed direction from that observed near the compression face/endwall intersection. This vortex is convected by the primary flow into the viscous wake and maintains its integrity well downstream of the strut, as indicated by the measured pitot pressure contours in Fig. 5.

Conclusions

A combined experimental and numerical investigation of supersonic strut/endwall interactions in an annular duct has been conducted. Good agreement between the experimental and numerical results has been obtained. This investigation has shown that the effect of endwall curvature is to increase the interaction strength for concave walls and to decrease the interaction strength for convex walls. A model for the vortical structure in the flow has been proposed that includes 1) a horseshoe vortex formed at the leading edge of the strut, 2) another horseshoe vortex formed at the trailing edge of the strut, 3) a vortex formed at the corner of the compression face of the strut/endwall intersection, which migrates away from the corner along the expansion face of the strut and eventually dominates the flow in the viscous wake of the strut, and 4) a corner vortex formed along the expansion face of the strut/endwall intersection, which is entrained into the trailing-edge horseshoe vortex. Although this vortex structure is well predicted upstream of the strut trailing edge by the prescribed turbulence model, the model underpredicts the strength of these vortices in the wake region directly behind the strut. Further improvements and/or modifications to the turbulence model will be required to improve overall agreement between predictions and experiment.

Acknowledgments

This work was supported by the NASA Lewis Research Center under Grant NAG3-376 and Contract NAS3-25266. David O. Davis was the project monitor. The computations were performed on the NAS Cray Y-MP at NASA Ames and the Cray Y-MP at NASA Lewis. The authors gratefully acknowledge NASA's support of this research.

References

[1] McCabe, A., "The Three-Dimensional Interaction of a Shock Wave with a Turbulent Boundary Layer," *Aeronautical Quarterly*, Vol. 17, Pt. 3, Aug. 1966, pp. 231–252.

[2] Korkegi, R. H., "On the Structure of Three-Dimensional Shock-Induced Separated Flow Regions," *AIAA Journal*, Vol. 14, No. 5, 1976, pp. 597–600.

[3] Kubota, H., and Stollery, J. L., "An Experimental Study of the Interaction Between a Glancing Shock Wave and a Turbulent Boundary Layer," *Journal of Fluid Mechanics*, Vol. 116, March 1982, pp. 431–458.

[4] Settles, G. S., and Lu, F. K., "Conical Similarity of Shock/Boundary-Layer Interactions Generated by Swept and Unswept Fins," *AIAA Journal*, Vol. 23, No. 7, 1985, pp. 1021–1027.

[5] Settles, G. S., and Kimmel, R. L., "Similarity of Quasiconical Shock Wave/Turbulent Boundary-Layer Interactions," *AIAA Journal*, Vol. 24, No. 1, 1986, pp. 47–53.

[6] Settles, G. S., and Dolling, D. S., *Swept Shock Wave/Boundary-Layer Interactions: A Survey*, edited by M. J. Hemsch and J. N. Nielsen, Vol. 104, Progress in Astronautics and Aeronautics, AIAA, New York, 1986, pp. 297–379.

[7] Alvi, F. S., and Settles, G. S., "Physical Model of the Swept Shock Wave/Boundary-Layer Interaction Flowfield," *AIAA Journal*, Vol. 30, No. 9, 1992, pp. 2252–2258.

[8] Lu, F. K., "Quasiconical Free Interaction Between a Swept Shock and a Turbulent Boundary Layer," *AIAA Journal*, Vol. 31, No. 4, 1993, pp. 686–692.

[9] Mee, D. J., Stalker, R. J., and Stollery, J. L., "Glancing Interactions Between Single and Intersecting Oblique Shock Waves and a Turbulent Boundary Layer," *Journal of Fluid Mechanics*, Vol. 170, Sept. 1986, pp. 411–433.

[10] Koide, S., and Stollery, J. L., "Effects of Junction Modifications on Sharp-Fin-Induced Shock Wave/Boundary Layer Interaction," AIAA Paper 93-2935, July 1993.

[11] Shizawa, T., Honami, S., Komiyama, F., Tanaka, Y., Sakata, K., Yanagi, R., Shindo, S., Murakami, A., Tanaka, A., Shiraishi, K., and Omi, J., "Effects of Boundary Layer Bleed on Swept-Shock/Boundary Layer Interaction," AIAA Paper 93-2989, July 1993.

[12] Horstman, C. C., "Computation of Sharp-Fin-Induced Shock Wave/Turbulent Boundary-Layer Interactions," *AIAA Journal*, Vol. 24, No. 9, 1986, pp. 1433–1440.

[13] Knight, D. D., Horstman, C. C., Shapey, B., and Bogdonoff, S., "Structure of Supersonic Turbulent Flow Past a Sharp Fin," *AIAA Journal*, Vol. 25, No. 10, 1987, pp. 1331–1337.

[14] Hung, C.-M., and Buning, P. G., "Simulation of Blunt-Fin Induced Shock Wave and Turbulent Boundary-Layer Interaction," AIAA Paper 84-0457, Jan. 1984.

[15] Panaras, A. G., "Numerical Investigation of the High-Speed Conical Flow Past a Sharp Fin," *Journal of Fluid Mechanics*, Vol. 236, March 1992, pp. 607–633.

[16] Knight, D. D., Badekas, D., Horstman, C. C., and Settles, G. S., "Quasiconical Flowfield Structure of the Three-Dimensional Single Fin Interaction," *AIAA Journal*, Vol. 30, No. 12, 1992, pp. 2809–2816.

[17] Lakshmanan, B., and Tiwari, S. N., "Study of Supersonic Intersection Flowfield at Modified Wing-Body Junctions," *AIAA Journal*, Vol. 31, No. 5, 1993, pp. 877–883.

[18] Brusniak, L., and Dolling, D. S., "Flowfield Dynamics in Blunt Fin-Induced Shock Wave Turbulent Boundary-Layer Interaction," AIAA Paper 93-3133, July 1993.

[19] Erengil, M. E., and Dolling, D. S., "Physical Causes of Separation Shock Unsteadiness in Shock Wave/Turbulent Boundary-Layer Interactions," AIAA Paper 93-3134, July 1993.

[20] Kleifges, K., and Dolling, D. S., "Control of Unsteady Shock-Induced Turbulent Boundary Layer Separation Upstream of Blunt Fins," AIAA Paper 93-3281, July 1993.

[21] Bogdonoff, S. M., and Stokes, W. L., "Crossing Shock Wave Turbulent Boundary Layer Interactions—Variable Angle and Shock Generator Length Geometry Effects at Mach 3," AIAA Paper 92-0636, Jan. 1992.

[22] Williams, K. E., and Hingst, W. R., "The Effect of Varying Mach Number on Crossing, Glancing Shocks/Turbulent Boundary-Layer Interactions," AIAA Paper 91-2157, June 1991.

[23] Davis, D. O., and Hingst, W. R., "Surface and Flow Field Measurements in a Symmetric Crossing Shock Wave/Turbulent Boundary Layer Interaction," AIAA Paper 92-2634, June 1992.

[24] Garrison, T. J., and Settles, G. S., "Flowfield Visualization of Crossing Shock-Wave/Boundary-Layer Interactions," AIAA Paper 92-0750, Jan. 1992.

[25] Garrison, T. J., and Settles, G. S., "Interaction Strength and Model Geometry Effects on the Structure of Crossing-Shock Wave/Turbulent Boundary-Layer Interactions," AIAA Paper 93-0780, Jan. 1993.

[26] Garrison, T. J., and Settles, G. S., "Laser Interferometer Skin-Friction Measurements of Crossing-Shock Wave/Turbulent Boundary-Layer Interactions," AIAA Paper 93-3072, July 1993.

[27] Narayanswami, N., Knight, D., Bogdonoff, S. M., and Horstman, C. C., "Crossing Shockwave-Turbulent Boundary Layer Interactions," AIAA Paper 91-0649, Jan. 1991.

[28] Reddy, D. R., "3-D Navier–Stokes Analysis of Crossing, Glancing Shocks/Turbulent Boundary Layer Interactions," AIAA Paper 91-1758, June 1991.

[29] Harloff, G. J., Williams, K. E., and Gessner, F. B., "Numerical Investigation of Supersonic Flow About Struts of Various Thicknesses in an Annular Duct," *AIAA Journal* (to be published).

[30] Williams, K. E., Gessner, F. B., and Harloff, G. J., "Design and Operation of a Supersonic Annular Flow Facility," *AIAA Journal*, Vol. 32, No. 7, 1994, pp. 1528–1531.

[31] Allen, J. M., "Impact Probe Displacement in a Supersonic Turbulent Boundary Layer," *AIAA Journal*, Vol. 10, No. 4, 1972, pp. 555–557.

[32] Strack, S. L., "Supersonic Pitot Tube Measurements at an Angle of Attack," *AIAA Journal*, Vol. 2, No. 4, 1964, pp. 778, 779.

[33] Chan, Y. L., "A Study of Local Flow Behavior in a Streamwise Corner of a Rectangular Diffuser," Masters Thesis, Dept. of Mechanical Engineering, Univ. of Washington, Seattle, WA, 1980.

[34] Cooper, G. K., and Sirbaugh, J. R., "PARC Code: Theory and Usage," Arnold Engineering Development Center, AEDC-TR-89-15, Arnold AFB, TN, Dec. 1989.

[35] Baldwin, B. S., and Lomax, H., "Thin Layer Approximation and Algebraic Model for Separated Turbulent Flows," AIAA Paper 78-257, Jan. 1978.

[36] Thomas, P. D., "Numerical Method for Predicting Flow Characteristics and Performance of Nonaxisymmetric Nozzles—Theory," NASA CR 3147, Sept. 1979.

[37] Steinbrenner, J. P., Chawner, J. R., and Fouts, C. L., "The Gridgen 3D Multiple Block Grid Generation System," Wright Patterson Development Center, WRDC-TR-90-3022, Vols. 1 and 2, Wright Patterson AFB, OH, July 1990.

[38] Henderson, T., Huang, W., Lee, K., and Choo, Y., "Three-Dimensional Navier–Stokes Calculation Using Solution Adaptive Grids," AIAA Paper 93-0431, Jan. 1993.